Analysis and Experiments on the Force Capabilities of Centripetal-Force-Actuated Microrobotic Platforms

Panagiotis Vartholomeos, *Member, IEEE*, and Evangelos Papadopoulos, *Senior Member, IEEE*

***Abstract*—This paper studies the capabilities of a microrobotic platform, driven by vibrating motors, to generate and impart micromanipulation forces of desired type and magnitude. First, an analysis is carried out on the nature of the actuation forces of the motion mechanism of the platform. The results demonstrate that the oscillating nature of these forces does not allow their direct use for micromanipulations. Consequently, further analysis is conducted to identify the conditions, under which the platform's actuation forces can be exploited for micromanipulations. To this end, a dynamic model of a single-dimensional pushing operation is developed, comprising the dynamics of the platform, the manipulator and the object. It is demonstrated by simulation that the forces imparted on the manipulated object depend on the physical parameters of the platform-manipulator system. Accordingly, a set of nonlinear equations involving platform-manipulator system parameters, is formulated that describes the conditions for developing micromanipulation forces of appropriate type and magnitude. The solution of this set of equations yields a range of parameter values, which are used as guidelines in the design and construction of a manipulator that is capable of applying smooth and controllable forces to manipulated objects. Using the parameter values suggested by the developed analysis, a needle type manipulator, appropriate for force feedback applications, is designed, built, and mounted on an experimental prototype of the microrobotic platform. Using this manipulator, experiments demonstrate the force capabilities of the microrobotic platform and verified the analytical and simulation results.**

***Index Terms*—Force feedback, micromanipulation, microrobotics, vibrating micromotors.**

I. Introduction

DURING the past decade, microrobotics has become an increasingly important field of research. Several domains of application, such as microassembly, microbiology, biotechnology, microscopy, and optoelectronics, employ miniaturized or microrobotic platforms carrying a variety of novel tools that can probe or manipulate specimens of micrometer dimensions [1]. Therefore, extensive research has been conducted on the design and realization of autonomous, dexterous, microrobotic systems employing a number of cooperating microrobots and micromanipulators. These are capable for nanometric precision, and offer flexibility and a wide mobility range.

The key issue in autonomous microrobotic systems is the actuation mechanism that they employ. This is responsible for their precision and their motion capabilities. In addition, it determines the power consumption, and consequently, their autonomy. Conventional motion mechanisms, such as motors and wheels, do not lend themselves to micropositioning tasks due to the increasing significance of frictional phenomena such as the stick-slip and the Stribeck effect, and to the large mechanical tolerances of the actuation mechanisms [2], [3]. Hence, nonconventional actuation mechanisms have to be employed for locomotion and manipulation that do not incorporate moving mechanical parts into their kinematic chain, i.e., from their base to their end-effector. These actuation mechanisms are often based either on inertial principles or use induced strain actuators (smart materials such as piezoelectric actuators, shape memory alloys, etc.), and combine submicrometer resolution motion with the speed virtues of coarse positioning. The most popular micropositioning motion mechanism is the stick-slip principle, which is implemented using piezoelectric actuators [4]. This principle is employed by the microrobots presented in [5] and [6]. These 3 DOF platforms are capable of positioning accuracy of less than 200 nm, and of speeds up to a few millimeters per second. Both locomotion and manipulation modules incorporated in these platforms employ the stick-slip principle. Another type of motion mechanism, also based on piezoelectric actuation, is the impact drive (a variant of the stick-slip) employed by the microrobotic platform Avalon [7], [8]. Again, both locomotion and manipulation was based on piezoelectric actuation. This platform allows for positioning accuracy of approximately 3 μm and develops speeds up to 1 mm/s. A different motion mechanism also based on piezoactuators is employed by the NanoWalker microrobot [9], [10]. The first prototypes of this microrobot were capable for minimum steps of the order of 30 nm, and demonstrated a maximum displacement rate of 200 mm/s. This platform used a scanning tunneling microscope (STM) tip for micromanipulation. Also interesting is the walking principle presented in [11] and [12]. Possibly, MiCRoN is the most advanced example of a microrobotic platform, employing piezoelectric actuators, and having an integrated micromanipulator [13], [14].

Although piezoelectric actuators tend to be the favored smart material for micropositioning and do provide the required positioning resolution and actuation response, they suffer from

Manuscript received July 18, 2007; revised December 12, 2007. This paper was recommended for publication by Associate Editor B. Nelson and Editor K. Lynch upon evaluation of the reviewers' comments. This work was supported in part by the European Social Fund (75%) and in part by the National Resources (25%)—(EPEAEK II)—HRAKLEITOS.

The authors are with the Department of Mechanical Engineering, National Technical University of Athens, Athens 15780, Greece (e-mail: barthol@central.ntua.gr; egpapado@central.ntua.gr).

Color versions of one or more of the figures in this paper are available online at http://ieeexplore.ieee.org.

Digital Object Identifier 10.1109/TRO.2008.919298

complex power units that are expensive and cumbersome and do not easily allow for nontethered operation. Embedding electronics in microrobotic platforms often result in excessive heating problems.

We proposed a simple and compact microrobot, which employs a novel actuation mechanism based on vibrating micromotors [15]. According to the developed analysis, the microrobotic platform is able to perform translational and rotational sliding with submicrometer positioning accuracy and velocities up to 2 mm/s [16]. All the components of the mechanism, including its driving units, are of low cost and readily available.

The target applications of this microrobotic platform are either: 1) *industrially oriented* such as the assembly of spatial (3-D) miniature devices and microelectromechanical system (MEMS) incorporating heterogeneous parts (Si, glass, ceramic, etc.) or 2) *biomedically oriented*, such as cell manipulation [13], sperm injection, the assembly of scaffolds for tissue engineering [19], etc. To this end, the platform has to execute, with submicrometer precision, a range of tasks such as pushing, positioning, cutting, or gluing of micro- and miniature components, whose weight ranges from a few milligrams to a few grams. Most of these microapplications, at the moment, are not standardized and involve a great degree of uncertainty. Therefore, a manipulation system, composed of a few mobile microrobots equipped with tools, is more efficient and has increased rates of success compared to a microfabrication station comprising a number of micromanipulators mounted on static bases (like in the car industry).

The aforementioned microrobot platforms, apart from their motion capabilities, must exhibit adequate force capabilities to allow for a range of manipulation tasks to be accomplished. Depending on the type of the application, micromanipulation forces may range from a few micronewtons to a few hundred millinewtons [17], [18], [19]. Forces of very small magnitude (i.e., of the order of micronewtons) are usually generated by the actuator that drives the microtool (e.g., the actuator of a microgripper). However, forces of larger scale should be provided by the motion mechanism of the platform itself.

The thrust of this paper is the exploitation of the centripetal-force actuation mechanism described in [15], in order to generate and transmit low ripple, controllable forces within a useful range of values for micromanipulation purposes. To this end, the dynamics of the system platform–manipulator object are analyzed and studied. Conditions for impulse-free force transmission are mathematically expressed, which when solved numerically, yield parameter values that result in controlled, impulse-free, low ripple, manipulation forces. The theoretical results are first verified through simulations. Based on the analytically derived design guidelines, a needle-type manipulator is designed and built. The manipulator is mounted on the microrobotic platform and force experiments are conducted that verify the theoretical results. It is shown experimentally that the platform is capable of applying micromanipulation controllable forces within the range of 10–300 mN.

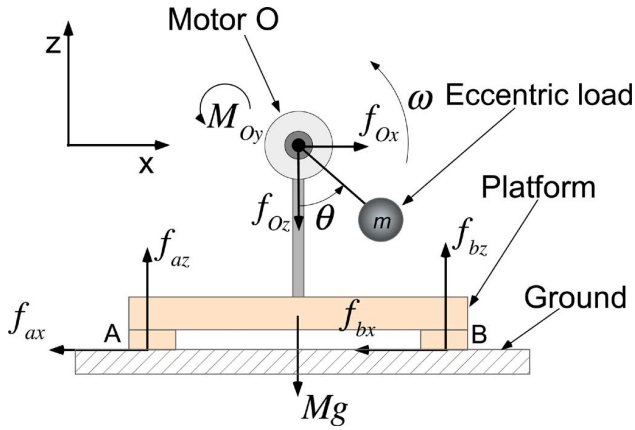

Fig. 1. Simplified 1 DOF platform with a rotating mass m.

II. Platform's Motion Principle and Dynamics

A. Motion Principle

The novel actuation principle of the microrobot is elaborated in [15] and [16]. A brief description of the physics that govern the motion principle is given here. To this end, a simplified 1 DOF mobile platform of mass M is used, whose motion mechanism is made of an eccentric mass *m,* rotated by a platform-mounted motor *O*, as shown in Fig. 1. One cycle of operation is completed when the mass *m* has described an angle of 360°.

Gravitational and centripetal forces exerted on the rotating mass are resolved along the *x–z* axis to yield

$$f_{Ox} = mr\omega^2 \sin\theta \tag{1a}$$

$$f_{Oz} = -mg - mr\omega^2 \cos\theta \tag{1b}$$

where g is the acceleration of gravity and r is the length of the link between m and *O* (see Fig. 1). Using a simplified static–kinetic friction model to describe the motion of the platform along the *x*- and *z*-axis results in the following equations

$$M\ddot{x} = f_{Ox} - f_{fr} = f_{Ox} - (f_{ax} + f_{bx}) \tag{2a}$$

$$f_{az} + f_{bz} + (-Mg + f_{Oz}) = 0 \tag{2b}$$

where *M* is the mass of the platform, f_{fr} is the Coulomb friction force, and all other forces are defined in Fig. 1.

For counterclockwise rotation of the eccentric mass m, the equations of motion of the platform are numerically simulated to yield the results displayed in Fig. 2. These are plotted as a function of the angle θ of the eccentric mass. Fig. 2(c) clearly displays the fact that a net displacement of the platform occurs and that motion is induced. Moreover, Fig. 2(c) demonstrates that, for a counterclockwise rotation of the motor, the platform of Fig. 1 exhibits a net displacement along the positive *x*-axis.

Equation (1) suggests that if the angular speed ω were less than a critical value ω_c, the platform would not slide because the horizontal actuation force f_{Ox} would be canceled by the frictional forces at the platform contact points A and B. However, if the angular speed ω is greater than ω_c, as in the simulation example, then at a critical angle θ_1, the horizontal actuation force f_{Ox} overcomes the Coulomb friction forces applied to the two contact points, [16]. In this case, as shown in Fig. 2, the platform begins to slide along the positive *x*-axis. When *m* passes

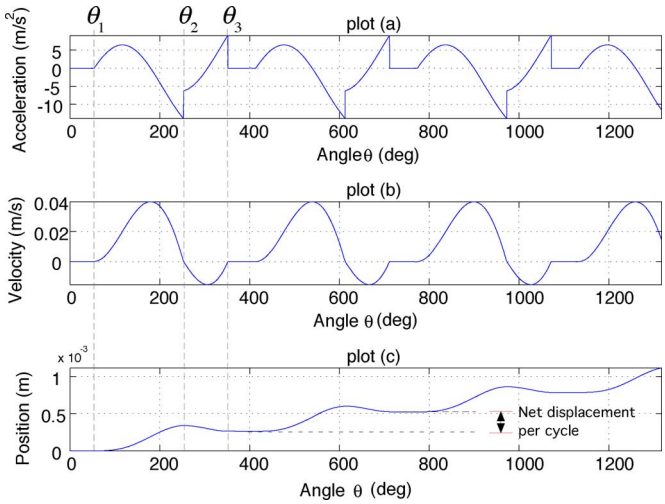

Fig. 2. Simulation results. (a) Acceleration. (b) Velocity. (c) Position along the x-axis as a function of the actuation angle.

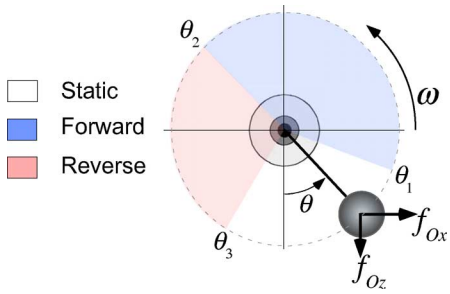

Fig. 3. Complete cycle of rotation of the eccentric mass m.

the highest point (at $\theta = 180^\circ$), friction forces, together with actuation forces, tend to decelerate the platform, and eventually, at an angle θ_2 change its direction of motion. As friction still increases, reverse motion is decelerated, and finally, the platform is brought to a stop at an angle θ_3. Fig. 3 demonstrates the cycle of rotation of the eccentric mass m and associates the angle θ with the motion state of the platform.

It is observed that the forward motion of the platform takes place when the rotating eccentric mass m is at the second and third quadrant of the cycle, i.e., when the vertical reactions are low, see (1). In contrast to this, the reverse motion takes place in the third and fourth quadrant, that is, when the vertical reactions increase. Therefore, the forward displacement is greater than the reverse one and the resultant displacement per cycle is positive.

It has been shown analytically that the single-dimensional motion step that the platform exhibits over a cycle can be made arbitrarily small depending on the actuation speed ω [16]. Accordingly, it has been demonstrated that the platform's motion resolution can reach submicrometer accuracy [15], [16]. In general, its resolution is hindered by the limited resolution of the electronics and by the nonuniform distribution of the coefficient of friction μ between surface and the contact points of the platform.

B. Platform Dynamics

The actuation principle mentioned earlier was employed in the design of a 3 DOF microrobot, [15], as shown schematically

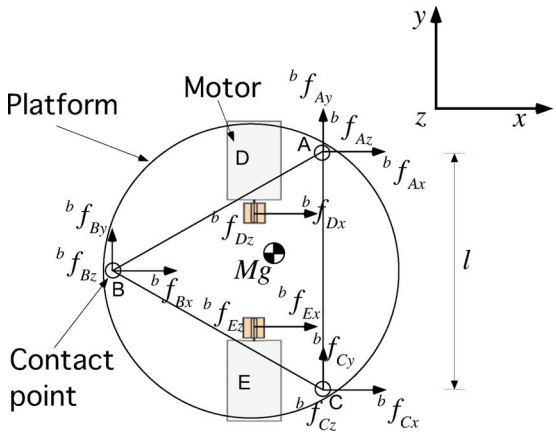

Fig. 4. Forces applied on the 2 DOF platform: top view.

TABLE I
PLATFORM DESIGN PARAMETERS

Parameter	Value	Parameter	Value
r $[m]$	0.00177	l $[m]$	0.05
m $[kg]$	0.00021	h_0 $[m]$	0.004
M $[kg]$	0.12	μ [-]	0.5

in Fig. 4. On the top of the platform, two centripetal-force actuators are mounted. The platform is capable of moving along the body-fixed x-axis and of rotating about its center of mass (CM) depending on the sense of rotation of the actuators.

The actuation forces generated by the two vibrating motors are given by

$$\left.\begin{aligned} {}^b f_{ix} &= -m_i r_i \omega_i^2 \sin\phi_i \sin\theta \\ {}^b f_{iz} &= -m_i g - m_i r_i \omega_i^2 \cos\theta \end{aligned}\right\}, \qquad i = \{D, E\} \tag{3}$$

where subscripts $i = \{D, E\}$ correspond to the two motors, $\omega_i = \dot{\theta}_i$ is motor's i angular velocity, r_i is the eccentricity of the imbalance mass m_i, and $\phi_i = \{90^\circ, -90^\circ\}$.

The dynamics of the platform are described by [20]

$$M\dot{\mathbf{v}} = \mathbf{R}\sum_i {}^b\mathbf{f}_i, \qquad i = \{A, B, C, D, E\} \tag{4a}$$

$${}^b\mathbf{I}\dot{\boldsymbol{\omega}}_p + {}^b\boldsymbol{\omega}_p \times {}^b\mathbf{I}\,{}^b\boldsymbol{\omega}_p = \sum_i ({}^b\mathbf{r}_i \times {}^b\mathbf{f}_i) + \sum_j {}^b\mathbf{n}_j,$$

$$i = \{A, B, C, D, E\}, \qquad j = \{D, E\} \tag{4b}$$

where $\mathbf{R}$ is a rotation matrix that resolves body-fixed free vectors to the inertial frame of reference, $\boldsymbol{\omega}_p$ is the platform angular velocity, ${}^b\mathbf{I}$ is its inertia matrix, and $\mathbf{v} = [\dot{x}, \dot{y}, \dot{z}]^T$ is its CM velocity wrt the inertial frame. The left superscript b denotes a body-fixed frame, while a missing left superscript denotes the inertial frame. The subscripts $i = \{A, B, C\}$ correspond to the three contact points of the platform. During planar motion analysis, (4)b can be simplified.

According to design specifications given in [15], a set of parameters was selected and is presented in Table I.

In this table, h_0 is the distance between an actuator's axis and the ground and l is the length of the side of the triangular base of the platform (see Fig. 4).

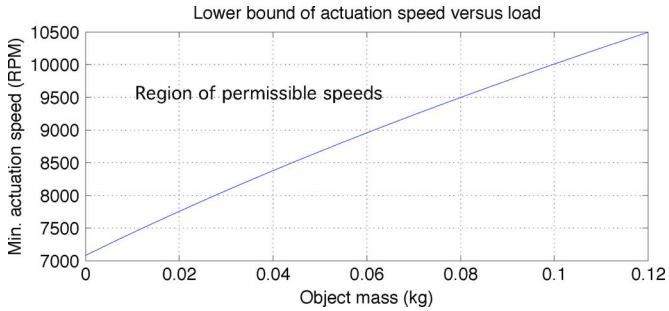

Fig. 5. Minimum actuation speed $\omega_{c\_\min}$ versus moving object mass.

III. Force Analysis

Many micromanipulation processes are currently executed by human operators, and consequently, suffer from low repeatability and long execution times. To substitute the human operator with one or more microrobots, the design must ensure that the microrobots exert controlled, low ripple forces on the objects. For this purpose, it is necessary to analyze the platform's force capabilities. The first step is to calculate an upper bound on the load the platform may carry and on the forces it may impart on an object. This is found by calculating the minimum required actuation speed $\omega_{\min}$ for pushing an object of mass M_O. To this end, it is assumed that an object of mass M_O is attached to the platform. Both actuators rotate at the same speed. The expression for $\omega_{\min}$ is found by considering the limiting case where motion is impeding and friction forces have reached the static limit:

$$ {}^{b}f_{Ax} + {}^{b}f_{Bx} + {}^{b}f_{Cx} = \mu({}^{b}f_{Az} + {}^{b}f_{Bz} + {}^{b}f_{Cz}) + \mu g M_O. \tag{5}$$

Substituting (3) into (5) and solving for ω yields

$$\omega_c = \left(\frac{-\mu g(M + M_O + 2m)}{2mr(\mu\cos\theta - \sin\theta)}\right)^{1/2}. \tag{6}$$

From (6), it is evident that the critical speed ω_c is a function of θ. The angle θ, at which the minimum ω_c occurs, is found and substituted into (6) to yield $\omega_{c\_\min}$:

$$\omega_{c\_\min} = \left(\frac{\mu g(M + M_O + 2m)}{2mr\sqrt{1+\mu^2}}\right)^{1/2}. \tag{7}$$

Fig. 5(a) depicts ω_c versus M_O. As expected, it shows that $\omega_{c\_\min}$ increases with the object mass. Note that Fig. 5 presents a theoretical actuation speed ω lower bound for generating sufficient forces to push an object of mass M_O. It does not take into account the actual nature of the forces imparted on a moving object or exerted on a wall. In the next section, a detailed analysis regarding the actual forces applied to a manipulated object is developed.

A. Forces Transmitted From the Platform to an Object

The platform is equipped with a needle-type micromanipulator as shown in Fig. 6(a). The 1-D dynamic model of the system platform–manipulator object is presented in Fig. 6(b).

The platform is constrained to move along the x-axis. With respect to the dynamics, two distinct cases are considered.

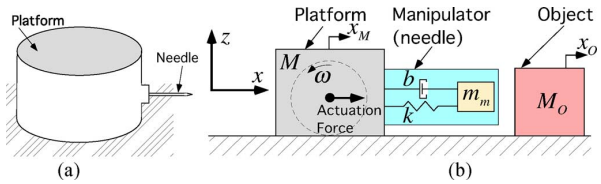

Fig. 6. Platform. (a) Schematic of platform and needle-type manipulator. (b) 1-D dynamic model of system platform–manipulator object.

1) Manipulator Tip is Not in Contact With the Object: In this case, the dynamics of the manipulator are neglected, i.e., $m_m = 0$.

The system is described by the two following equations of motion

$$M\ddot{x}_M = f_x - f_{fr\_M} \tag{8a}$$

$$M_O\ddot{x}_O = -f_{fr\_O} \tag{8b}$$

where f_{fr_M}, f_{fr_O} represent the Coulomb friction exerted on the platform and on the object, respectively, and are given by

$$f_{fr\_M} = \begin{cases} -f_{Cp}\mathrm{sgn}(\dot{x}_\mathrm{M}), & \dot{x}_\mathrm{M} \neq 0 \\ (f_x - f_k - f_b), \|f_x - f_k - f_b\| < f_{Cp}, & \\ \dot{x}_\mathrm{M} = 0 \quad \text{and} \quad \ddot{x}_\mathrm{M} = 0 & \\ -f_{Cp}\mathrm{sgn}(f_x - f_k - f_b), \|f_x - f_k - f_b\| \geq f_{Cp}, & \\ \dot{x}_\mathrm{M} = 0 \quad \text{and} \quad \ddot{x}_\mathrm{M} \neq 0 & \end{cases} \tag{9}$$

and

$$f_{fr\_o} = \begin{cases} -f_{Co}\mathrm{sgn}(\dot{x}_o), & \dot{x}_o \neq 0 \\ (f_k + f_b), \|f_k + f_b\| < f_{Co}, & \dot{x}_o = 0, \\ \ddot{x}_o = 0 & \\ -f_{Co}\mathrm{sgn}(f_k + f_b), \|f_k + f_b\| \geq f_{Co}, & \\ \dot{x}_o = 0, \quad \ddot{x}_o \neq 0 & \end{cases} \tag{10}$$

where $f_{Cp} = \mu(Mg + f_z)$ is the Coulomb static limit of the platform and $f_{Co} = \mu M_O g$ of the object and $\mathrm{sgn}()$ is the signum function. Actuation forces f_x, f_z are given by

$$f_x = \sum_i f_{ix}, i = \{D, E\} \tag{11}$$

$$f_z = \sum_i f_{iz}, i = \{D, E\} \tag{12}$$

where f_{ix}, f_{iz} are given in (3).

2) Manipulator Tip is in Contact With the Object: In this case, the dynamics of the manipulator are taken into account. The object is considered to be rigid. The equations of motion for the platform and object are

$$M\ddot{x}_M = f_x - f_k - f_b - f_{fr\_M} \tag{13a}$$

$$M_O\ddot{x}_O = f_k + f_b - f_{fr\_O} \tag{13b}$$

$$f_k = k(x_M - x_O) = k\Delta x$$

$$f_b = b(\dot{x}_M - \dot{x}_O) = b\Delta\dot{x} \tag{14}$$

where Δx is the deformation of the manipulator.

TABLE II
MANIPULATOR AND OBJECT PARAMETERS

Parameter	Value	Parameter	Value
k [N/m]	2.5×10^6	b [Ns/m]	200
M_O [kg]	0.001	ω [rad / s]	900

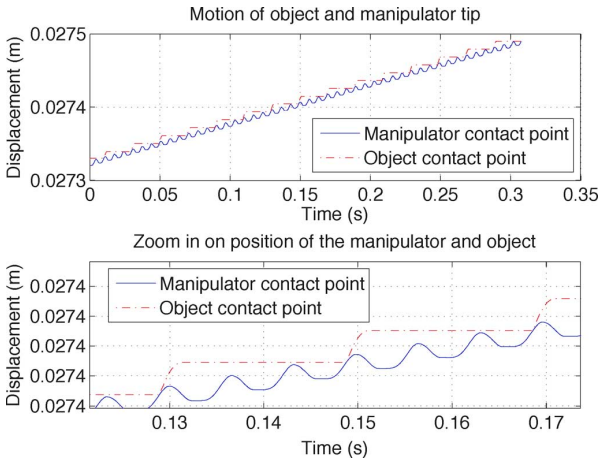

Fig. 7. Platform pushing an object. (a) Position of platform and object. (b) Zoom-in on three consecutive cycles of position of platform and object.

Equations (13) are used to simulate various pushing scenarios in MATLAB. Typical simulation parameters for a pushing scenario with a needle-type manipulator are given in Tables I and II.

In the first case studied, the platform comes into contact with the free to move object, and pushes it along the positive x-axis. Fig. 7 depicts simulation results of the platform and object response during the pushing operation.

The solid line represents the response of the manipulator and the dashed line represents the response of the object. The first plot depicts the displacement of the manipulator's tip and of the object. The second plot zooms-in on three successive cycles of the first plot. It is observed that the platform bounces off the object. Fig. 8 shows the forces exerted on the object by the manipulator tip. Observing Fig. 8(a), one can see that these are of impulsive nature. The second plot zooms-in on a single impulse. Note that the forces applied to the object are always positive, i.e., pushing forces. This is expected since the platform manipulator is not able to pull.

The next example demonstrates the case of the platform pushing against a totally constrained object, i.e., a wall. From the first plot in Fig. 9, it is observed that the manipulator tip bounces off the wall and the platform retreats almost three cycles back. As in the previous case, the platform exerts on the wall impulsive forces and oscillates close to it. Note that, in Fig. 9, the manipulator's tip (solid line) erroneously seems to cross the wall (dashed line) when in contact. This happens due to the contact detection tolerances set during simulation.

In most cases, impulsive forces are undesirable because they result in wear and eventually in damage of the manipulated object. Furthermore, the fluctuation of impulses cannot be predicted and controlled easily. Hence, in most manipulation cases, the forces exerted on the manipulated object have to be controllable, impulse-free, and subject to low ripple. Therefore, an appropriate design is desired to eliminate impulses during manipulation.

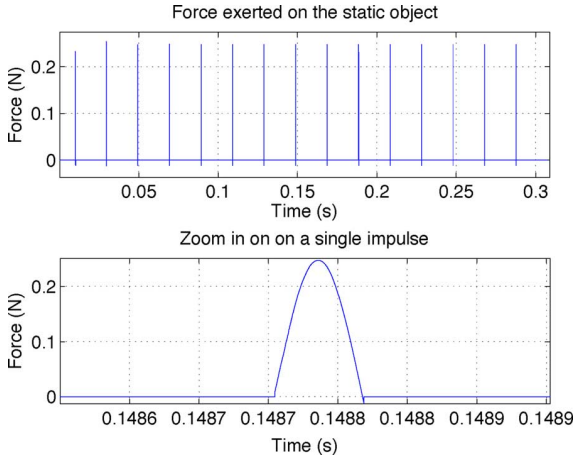

Fig. 8. Impulsive forces applied on the object during bouncing.

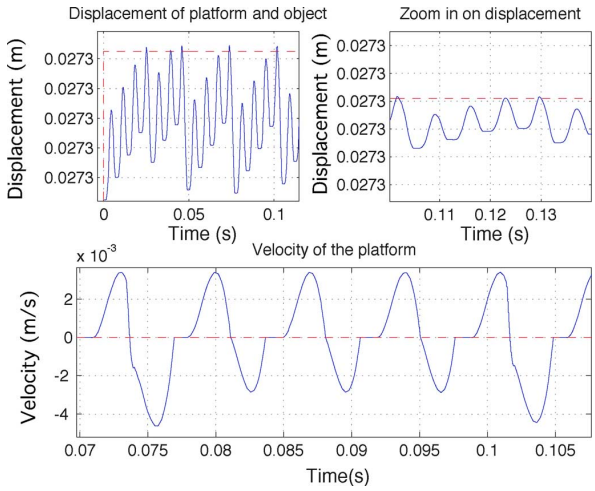

Fig. 9. Displacement and velocity of the platform bouncing against a wall.

B. Impulse Reduction and Ripple Attenuation

For reasons of simplicity and to exploit the merits of analytical solutions, the following analysis assumes that the manipulator pushes against a wall (object totally constrained).

Impulsive forces reduction: The ideal force transmission is defined as the one where the platform smoothly pushes the object, remains attached to it, and no bouncing takes place, i.e., no impulsive forces are exerted on the object. This is a challenging goal due to the vibrating nature of the actuation mechanism. Ideal force transmission can be accomplished if the platform oscillates about a fixed point O, while the manipulator tip remains attached to the object, i.e., the manipulator should always be deformed as shown in Fig. 10.

Fig. 10 presents a single cycle of operation. The top schematic shows the manipulator at its minimum deformation x_{θ_1}. As the eccentric mass rotates, the manipulator reaches its maximum

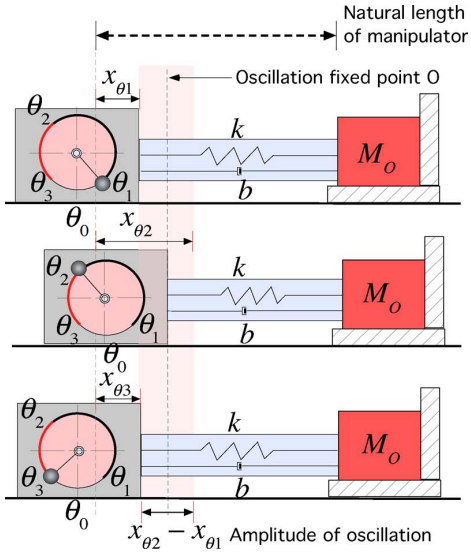

Fig. 10. Steady-state operation. Manipulator tip remains attached to the object while platform oscillates about a fixed point O.

deformation x_{θ_2} at angle θ_2, shown in the middle schematic. Next, the manipulator again reaches its minimum deformation $x_{\theta_3} = x_{\theta_1}$ at angle θ_3 and stays deformed until the rotating mass reaches angle θ_1 again. Hence, ideal force generation can be attained if there exists a steady-state operation, where the forward displacement of the platform is equal to the reverse one. To express mathematically this condition, it is convenient to break (13) a into two parts.

1) Platform Equation of Forward Motion, i.e., for $\dot{x} \geq 0$: Equation 15 as shown at bottom of the page.

Solving the linear ordinary differential equation (ODE) (15) with respect to the displacement x_{fwd} yields the following analytical solutions, for x_{fwd} and the velocity $\dot{x}_{\mathrm{fwd}}$

$$\begin{aligned} x_{\mathrm{fwd}}(\theta) = &- \frac{g(2m+M)\mu}{k} + e^{-b\theta/2M\omega}(c_1 \cos\gamma + c_2 \sin\gamma) \\ &- \frac{2mr\omega^2 \cos\theta((k\mu+\omega(b-M\mu\omega))\cos\theta_1}{(b\omega)^2+(k-M\omega^2)^2} \\ &+ \frac{(-k+\omega(b\mu+M\omega))\sin\theta_1)}{(b\omega)^2+(k-M\omega^2)^2} \\ &\times \frac{2mr\omega^2((k-\omega(b\mu+M\omega))\cos\theta_1}{(b\omega)^2+(k-M\omega^2)^2} \\ &+ \frac{(k\mu+\omega(b-M\mu\omega))\sin\theta_1)\sin\theta}{(b\omega)^2+(k-M\omega^2)^2} \end{aligned} \tag{16}$$

$$\begin{aligned} \dot{x}_{\mathrm{fwd}}(\theta) = &- \frac{b\, e^{-\frac{b\theta}{2M\omega}}(c_1 \cos\gamma + c_2 \sin\gamma)}{2M} \\ &+ e^{-b\theta/2M\omega}\left(\frac{c_2\sqrt{-b^2+4kM}\cos\gamma}{2M}\right. \\ &\left. - \frac{c_1\sqrt{-b^2+4kM}\sin\gamma}{2M}\right) \\ &+ \frac{2mr\omega^3 \cos\theta((k-\omega(b\mu+M\omega)\cos\theta}{(b\omega)^2+(k-M\omega^2)^2} \\ &+ \frac{(k\mu+\omega(b-M\omega\mu))\sin\theta_1)}{(b\omega)^2+(k-M\omega^2)^2} \\ &+ \frac{2mr\omega^3((k\mu+\omega(b-M\mu\omega))\cos\theta_1+}{(b\omega)^2+(k-M\omega^2)^2} \\ &+ \frac{(-k+\omega(b\mu+M\omega))\sin\theta_1)\sin\theta}{(b\omega)^2+(k-M\omega^2)^2} \end{aligned} \tag{17}$$

where the angles $\theta_1, \theta_2, \theta_3$ are defined in Fig. 3, c_1, c_2, are coefficients related to the initial conditions of (15) and are given in Appendix A, and

$$\begin{aligned} \theta &= \omega t \\ \gamma &= \frac{\sqrt{-b^2+4kM}}{2M\omega}. \end{aligned} \tag{18}$$

2) Platform Equation of Reverse Motion, i.e., for $\dot{x} < 0$: Equation 19 as shown at bottom of the page.

Solving the linear ODE (19) with respect to the displacement x_{rvr} yields the following analytical solutions, for x_{rvr} and the velocity$\dot{x}_{\mathrm{rvr}}$

$$\begin{aligned} x_{\mathrm{rvr}}(\theta) = &\frac{\mu(2m+M)g}{k} + e^{-b\theta/2M\omega}(c_3 \cos\gamma + c_4 \sin\gamma) \\ &+ \frac{2mr\omega^2 \cos\theta((k\mu-\omega(b+M\mu\omega))\cos(\theta_2+\theta_1)}{(b\omega)^2+(k-M\omega^2)^2} \\ &+ \frac{(k+\omega(b\mu-M\omega))\sin(\theta_2+\theta_1))}{(b\omega)^2+(k-M\omega^2)^2} \\ &+ \frac{2mr\omega^2((k+\omega(b\mu-M\omega))\cos(\theta_2+\theta_1)}{(b\omega)^2+(k-M\omega^2)^2} \\ &+ \frac{(-k\mu+\omega(b\mu-M\omega))\sin(\theta_2+\theta_1))\sin\theta}{(b\omega)^2+(k-M\omega^2)^2} \end{aligned} \tag{20}$$

$$\begin{aligned} &\ddot{x}_{\mathrm{fwd}}(t) + \frac{b}{M}\dot{x}_{\mathrm{fwd}}(t) + \frac{k}{M}x_{\mathrm{fwd}}(t) \\ &\quad = (-\mu(M+2m)g + 2mr\omega^2(\sin(\omega t)(\cos\theta_1 + \mu\sin\theta_1) + \cos(\omega t)(\sin\theta_1 - \mu\cos\theta_1)))/M - kx_{\theta 1}/M \end{aligned} \tag{15}$$

$$\begin{aligned} &\ddot{x}_{\mathrm{rvs}}(t) + \frac{b}{M}\dot{x}_{\mathrm{rvs}}(t) + \frac{k}{M}x_{\mathrm{rvs}}(t) \\ &= (\mu(M+2m)g + 2mr\omega^2(\sin(\omega t)(\cos(\theta_1+\theta_2) - \mu\sin(\theta_1+\theta_2)) + \cos(\omega t)(\sin(\theta_1+\theta_2) + \mu\cos(\theta_1+\theta_2))))/M - kx_{\theta 2}/M \end{aligned} \tag{19}$$

$$\dot{x}_{\rm rvr}(\theta) = -\frac{b\,e^{-\frac{b\theta}{2M\omega}}(c_3\,\cos\gamma + c_4\sin\gamma)}{2M} + e^{-b\theta/2M\omega}\left(\frac{c_4\sqrt{-b^2+4kM}\,\cos\gamma}{2M} - \frac{c_3\sqrt{-b^2+4kM}\sin\gamma}{2M}\right) + \frac{2mr\omega^3\cos\theta((k+\omega(b\mu-M\omega))\cos(\theta_2+\theta_1)}{(b\omega)^2+(k-M\omega^2)^2} + \frac{(-k\mu+\omega(b+M\mu\omega))\sin(\theta_2+\theta_1))}{(b\omega)^2+(k-M\omega^2)^2} - \frac{2mr\omega^3((k\mu-\omega(b+M\mu\omega))\cos(\theta_2+\theta_1)+}{(b\omega)^2+(k-M\omega^2)^2} \frac{(k+\omega(b\mu-M\omega))\sin(\theta_2+\theta_1))\sin\theta}{(b\omega)^2+(k-M\omega^2)^2} \quad (21)$$

where c_3, c_4 are coefficients related to the initial conditions of (19) and are given in Appendix A.

The following mathematical equations should be satisfied for steady-state operation to occur.

1) The forward displacement must be equal to the reverse displacement:

$$x_{\rm fwd}(\theta_1) = x_{\rm rvs}(\theta_3). \quad (22)$$

2) Motion toward the positive x-axis is impeding, i.e., friction at the contact points has reached its Coulomb level:

$$2mr\omega^2(\sin\theta_1 - \mu\cos\theta_1) = kx_{\rm fwd}(\theta_1) + \mu(M+2m)g. \quad (23)$$

3) The maximum displacement during forward motion is derived by setting $\theta = \theta_2$ in (16):

$$x_{\theta 2} = x_{\rm fwd}(\theta_2). \quad (24)$$

4) The platform velocity becomes zero when the deformation of the manipulator is equal to $x_{\theta 2}$. This condition is expressed by setting $\theta = \theta_2$ in (17):

$$\dot{x}_{\rm fwd}(\theta_2) = 0. \quad (25)$$

5) The maximum displacement during reverse motion is derived by setting $\theta = \theta_3$ in (20):

$$x_{\theta 3} = x_{\rm rvs}(\theta_3). \quad (26)$$

6) The platform velocity becomes zero when the deformation of the manipulator is equal to $x_{\theta 3}$. The condition is derived by setting $\theta = \theta_3$ in (21):

$$\dot{x}_{\rm rvs}(\theta_3) = 0. \quad (27)$$

It is convenient to write (22)–(27) in a functional form:

$$f_1(x_{\theta 1}, x_{\theta 3}) = 0$$
$$f_2(x_{\theta 1}, \theta_{\theta 1}) = 0$$
$$f_3(x_{\theta 1}, x_{\theta 2}, \theta_{\theta 1}, \theta_{\theta 2}) = 0$$
$$f_4(x_{\theta 1}, x_{\theta 2}, \theta_{\theta 1}, \theta_{\theta 2}) = 0$$

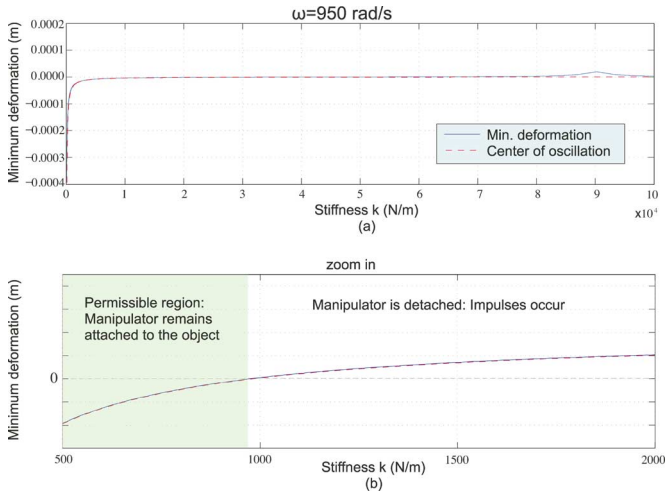

Fig. 11. (a) Manipulator minimum deformation versus stiffness. (b) Zoom-in.

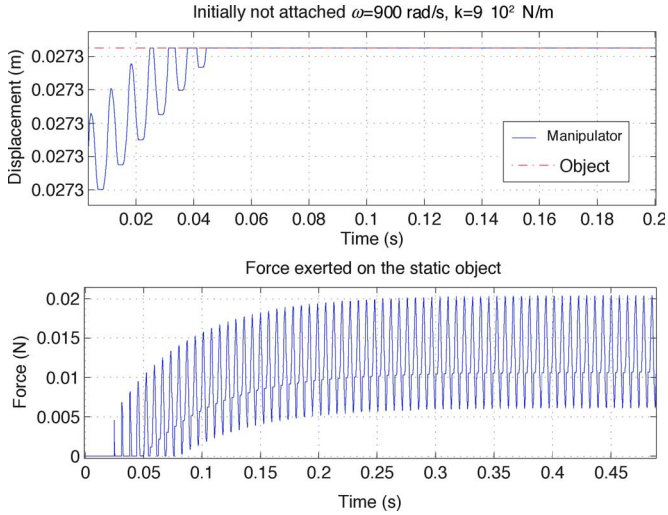

Fig. 12. Impulse-free displacement and force response.

$$f_5(x_{\theta 1}, x_{\theta 2}, x_{\theta 3}, \theta_1, \theta_2, \theta_3) = 0$$
$$f_6(x_{\theta 1}, x_{\theta 2}, x_{\theta 3}, \theta_1, \theta_2, \theta_3) = 0. \quad (28)$$

The system (28) of six nonlinear equations and six unknowns is solved for a range of manipulator stiffness values k and a range of actuation speed values ω. The rest of the parameters are considered to be known. Fig. 11 demonstrates the results of manipulator deformation versus manipulator stiffness k for $\omega = 900$ rad/s.

It is observed that there is a critical stiffness value $k_c = 980$ N/m, below which the manipulator tip remains continuously attached to the object throughout manipulation. The range of stiffness values below k_c is called the *permissible range*. This result constitutes a design guideline for attaining the desired manipulation operation.

Next, a simulation is conducted for $k < k_c$, and, in particular, for $k = 900$ N/m. The simulation scenario is the same as the one in Fig. 9, i.e., the manipulator pushes against a wall. Fig. 12 presents displacement and force results.

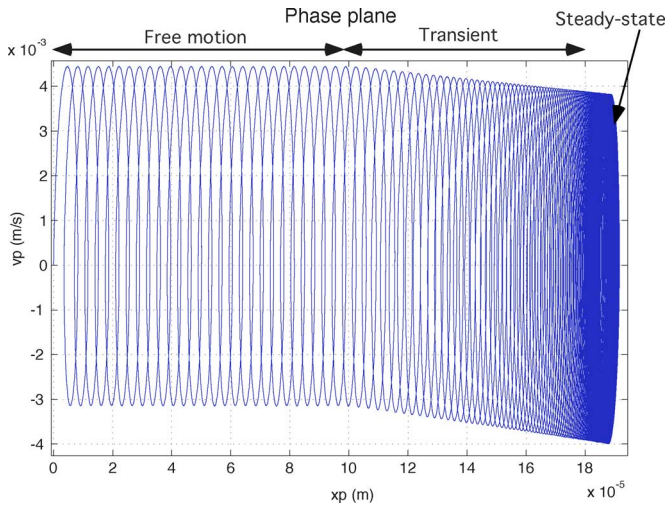

Fig. 13. Phase plane diagram for the platform's CM when $k < k_c$.

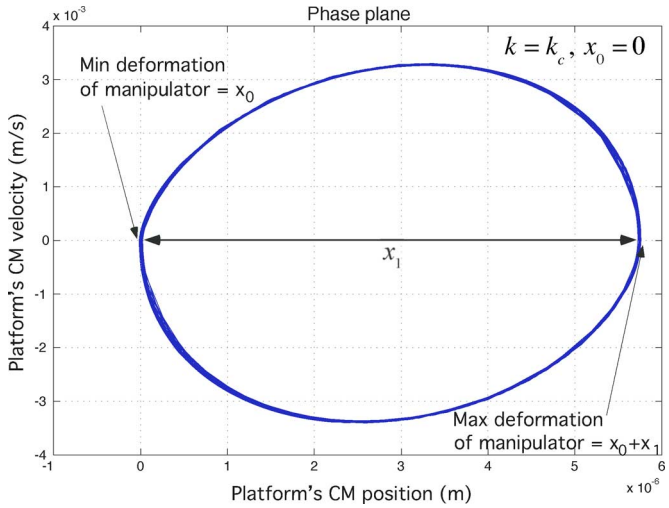

Fig. 14. Phase plane diagram for the platform's CM when $k = k_c$.

Initially, the manipulator tip is not in contact with the object. At $t = 0.025$ s, the manipulator tip comes into contact with the object and remains attached to it throughout the rest of the time. Evidently, the high impulses are eliminated and a forced oscillation occurs. Fig. 13 presents the corresponding phase plane diagram of the response of the platform's CM.

The *free motion* corresponds to the distance covered by the platform before it comes into contact with the object. Also, it is observed that the platform exhibits a *transient response*, during which a few detachments take place.

In order to have no transient response, the stiffness must be equal to k_c. The results for $k = k_c$ are depicted in Fig. 14. In this example the manipulator tip is initially attached to the object. It is observed that the transient response has been eliminated. As expected, for $k = k_c$, the minimum deformation of the manipulator is $x_0 = 0m$.

Although forces imparted to the object are impulse-free, they still suffer from a high amplitude ripple. Hence, the mean value of the force transmitted to the object must be regulated and the force amplitude ripple attenuated.

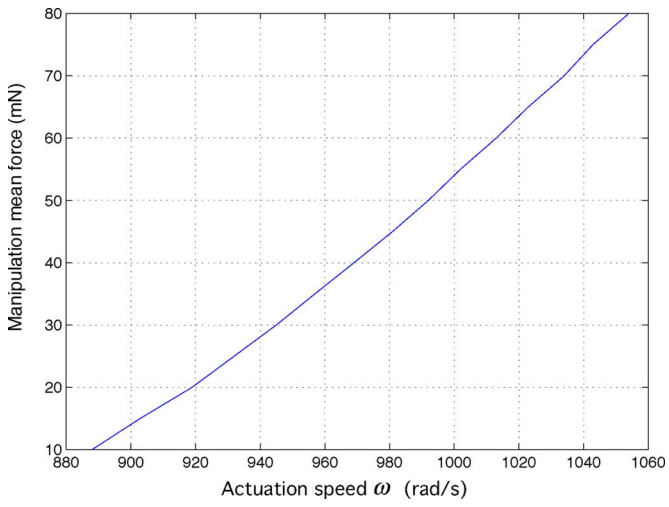

Fig. 15. Mean value of transmitted force as a function of actuation speed ω.

Regulation of force mean value: The forces transmitted to the object through the manipulator F_m are given by

$$F_m = \begin{cases} F_{m\_\mathrm{fwd}} = kx_{\mathrm{fwd}}(t) + b\dot{x}_{\mathrm{fwd}}(t), & \dot{x}(t) \geq 0 \\ F_{m\_\mathrm{rvs}} = kx_{\mathrm{rvs}}(t) + b\dot{x}_{\mathrm{rvs}}(t), & \dot{x}(t) < 0. \end{cases} \tag{29}$$

The mean force exerted on the object over a single cycle of operation is given by

$$F_{m\_\mathrm{mean}}(\omega) = \frac{\left(\omega/\theta_2 \int_0^{\theta_2} F_{m\_\mathrm{fwd}}(\theta)\, d\theta + \omega/\theta_3 \int_0^{\theta_3} F_{m\_\mathrm{rvs}}(\theta) d\theta\right)}{2}. \tag{30}$$

Next, the desired mean value of the transmitted force $F_{m\_\mathrm{mean\_des}}$ is set as a design requirement. This yields a seventh equation to be satisfied when solving the system of equations (28)

$$\begin{aligned} F_{m\_\mathrm{mean\_des}} - F_{m\_\mathrm{mean}} = 0 \Rightarrow \\ f_7(x_{\theta 1}, x_{\theta 2}, x_{\theta 3}, \theta_1, \theta_2, \theta_3, \omega) = 0. \end{aligned} \tag{31}$$

The solution of the augmented system of equations provides, among other solutions, the value for ω, for which $F_{m\_\mathrm{mean\_des}}$ is attained. Solving for a range of $F_{m\_\mathrm{mean\_des}}$ results in the graph depicted in Fig. 15.

A simulation is conducted for $\omega = 947$ rad/s and the force response is presented in Fig. 16. This response verifies the predictions of Fig. 15. Hence, we conclude that the mean value of the force transmitted to an object can be controlled by selecting appropriate actuations speeds. The next step is to reduce the ripple to an acceptable level.

Ripple attenuation: Appropriate values for k and ω are assigned so that the manipulator tip remains attached to the object and imparts to it a desired force mean value. Simulations are performed for a range of values of damping b. It is observed that the smaller the value of b is, the smaller the force ripple is. Fig. 17 depicts the force exerted on the object, when stiffness is

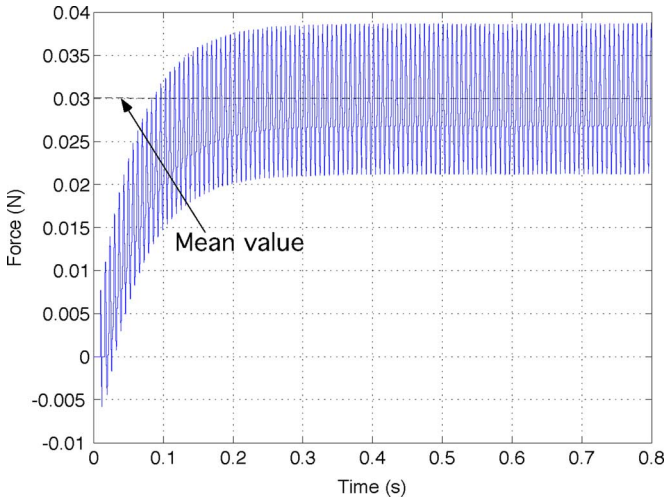

Fig. 16. Mean value of force transmitted to the object.

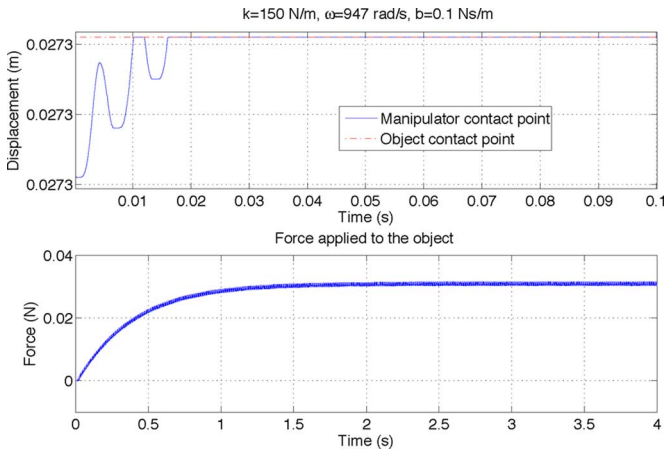

Fig. 17. Attenuated force ripple.

$k = 150$ N/m, actuation speed is $\omega = 947$ rad/s, and damping value $b = 0.01$ (N·s)/m.

It is observed that the ripple has been substantially reduced compared to the one in Fig. 16. It is also observed that the mean value of the force remains approximately 30 mN.

Hence, throughout the aforementioned analysis, it was demonstrated that appropriate selection of ω, k values and setting b as small as possible results in an impulse-free manipulation with low ripple and controlled mean value of the transmitted force.

IV. Force Generation Experiments

A prototype of the microrobotic platform, shown in Fig. 18, was constructed and experiments were conducted in order to verify the previous analysis and evaluate the force capabilities of the platform. During the experiments, the manipulator of the platform exerts forces on a stiff and static force sensor.

The experimental setup is presented in Fig. 19. It comprises a cylindrical ATI17 NANO six-axis force sensor, connected to a PC equipped with a NI DAQ Card 6036E, which performs A/D conversion, measuring the applied force.

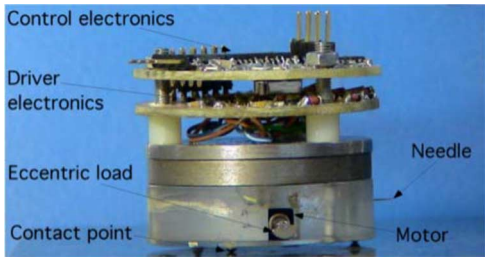

Fig. 18. Microrobot used in the experiments.

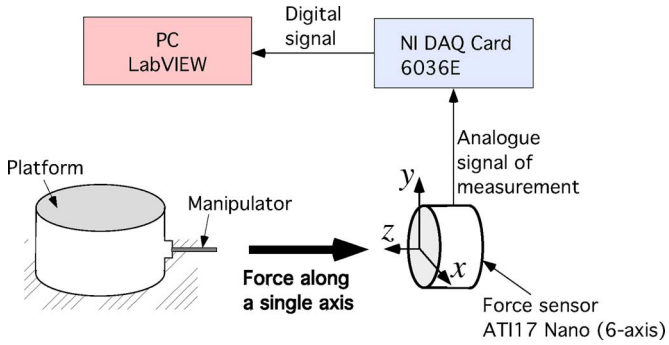

Fig. 19. Experimental setup for evaluation of the force capabilities of the platform.

A. Experiment 1: Manipulator Stiffness k is Greater Than k_c

In this experiment, the manipulator's stiffness is greater than the critical value $k_c = 980$ N/m given by (28). The manipulator is implemented using a steel pin having $k > 10$ kN/m. The steel pin is directly mounted on the platform as shown in Fig. 19.

The initial position of the platform allows for a 2 mm distance between the manipulator's tip and the force sensor. At $t = 0$ s, the microrobot commences linear motion and moves toward the force sensor. The two actuators operate synchronously at an angular speed $\omega_1 = 900$ rad/s. At $t_1 = 2.5$ s, the tip of the pin comes into contact with the surface of the force sensor, and exerts forces along the sensor's z-axis. At $t = 6.5$ s, the actuator speeds are reduced to $\omega_2 = 800$ rad/s. At $t = 11$ s, actuation stops. The forces measured during this experiment are presented in Fig. 20.

The first plot presents the forces that the manipulator exerted on the z-axis of the force sensor. The second plot depicts a zoom-in on these forces. We observe the following.

1) As predicted by the analysis in Section III, the forces exerted on a static object by a high stiffness manipulator are impulsive.
2) It is observed that the magnitude of the force exhibits random variations about a mean value. The randomness, which is related to the speed of the platform at the instant of the impact, was also observed in the simulation results, albeit the standard deviation about the mean value was smaller.
3) Furthermore, the experimental results demonstrate that the mean value of the impulses is related to the value of the actuators' rotation speed. The larger the speed ω is, the

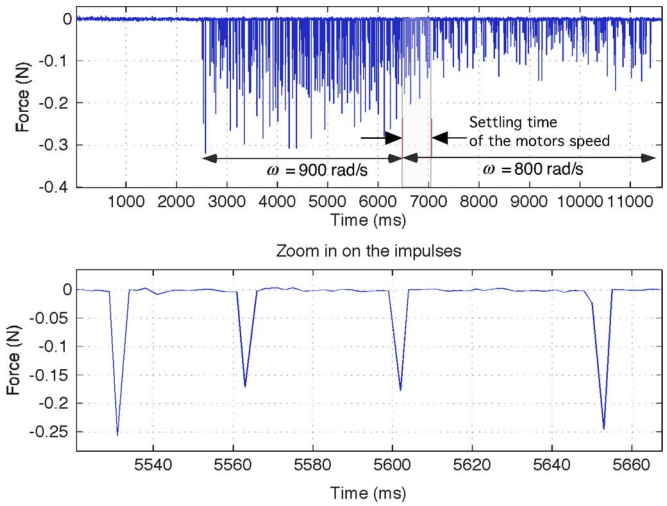

Fig. 20. First plot presents forces exerted on the object by the manipulator. The second plot depicts a magnified detail of the first plot.

greater the forces exerted on the object by the platform are.

4) It should also be noted that as shown in the first plot of Fig. 20, the impulses do not reduce instantly at $t = 6.5$ s, but, instead, they reach their new mean value at approximately $t = 7$ s. This delay reflects the settling time of the dc motors response, which is approximately 400 ms.
5) The impulse frequency is approximately one third of the actuation frequency. In other words, the platform bounces to the wall every three cycles of operation. This experimental result was also predicted by the simulation presented in Fig. 9.

B. Experiment 2: Manipulator Stiffness k is Less Than k_c

The goal of the second experiment is to test the force capabilities of the platform when its manipulator has stiffness $k < k_c$. The manipulator now is composed of a needle mounted on a base. This type of manipulator can be used to perform injection into cells, such as the Zebrafish embryo, whose diameter is approximately 800–1000 μm. In addition, the needle can be used for a variety of pushing operations on either static or moving objects. The needle, whose body diameter is approximately 300 μm and its tip diameter is approximately 30 μm, has stiffness much higher than k_c. Therefore, the first step is to design appropriately the base so that the needle–base system exhibits stiffness less than k_c. To this end, the base is an aluminum sheet onto which the needle is mounted. A local frame *x*–*y*–*z* is attached to the base as shown in Fig. 21.

When the needle imparts a force *P* on an object, the aluminum base exhibits a tip elastic deflection equal to Δz. The relation between *P* and Δz is given by

$$P = \frac{3EI}{\ell^3}\Delta z \tag{32}$$

where E is Young's modulus of aluminum, ℓ is the length of the sheet, and I is the area moment of inertia of the sheet about its

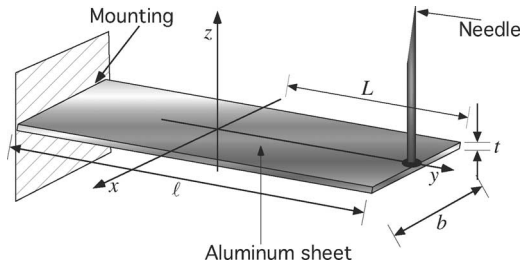

Fig. 21. Needle assembly design and dimensions.

TABLE III
PARAMETERS OF THE ALUMINUM BASE

Parameter	Value	Parameter	Value
E	70 [GPa]	ℓ	15 [mm]
T	100 [μm]	B	8 [mm]

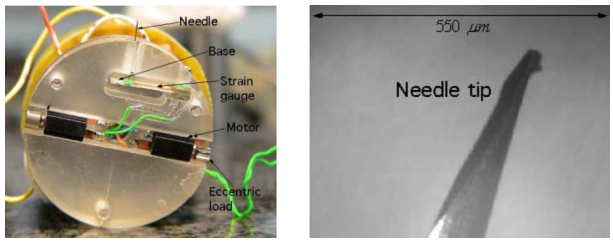

Fig. 22. (a) Platform underside. (b) Needle tip as seen with a microscope.

x-axis, given by

$$I = \frac{bt^3}{12} \tag{33}$$

where *b* is the aluminum sheet width and *t* its thickness. Equation (32) can be written as

$$P = k\Delta z \tag{34}$$

where

$$k = \frac{Ebt^3}{4\ell^3} \tag{35}$$

is the stiffness of the needle assembly. The values of the parameters in (35) are selected so that $k = 130$ N/m, and are presented in Table III.

A strain gauge was attached on the base to measure the 1 DOF compressive forces on the needle. The base–needle installation together with the strain gauge are depicted in Fig. 22(a). Note that the three contact points of the platform are not visible in Fig. 22(a) because the underside cover has been removed to facilitate the examination of the interior of the body. Fig. 22(b) shows the tip of the needle.

As in Experiment 1, the platform was driven toward the force sensor. The actuation speed was $\omega = 900$ rad/s. The needle tip reached the force sensor and started pushing. Fig. 23(a) presents the forces exerted on the object. The experiment is repeated with $\omega = 800$ rad/s. The results are demonstrated in Fig. 23(b).

As predicted by the developed analysis, for $k < k_c$, the manipulator remains attached to the object during operation, the forces exerted on the object are continuous, and the impulsive

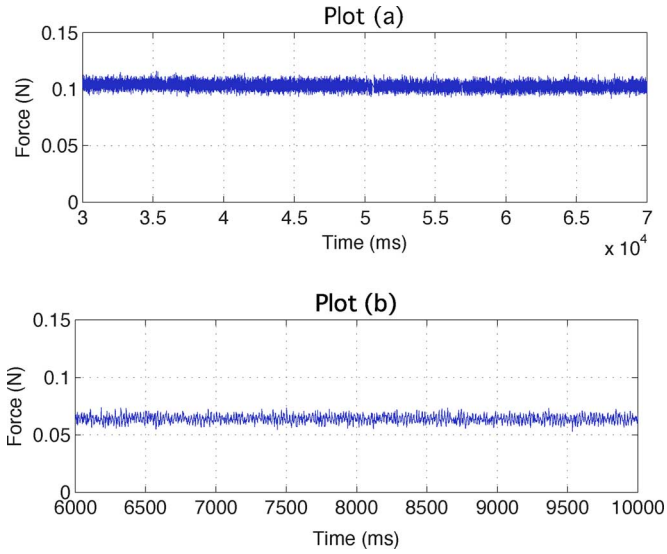

Fig. 23. Forces exerted on a static object when manipulator stiffness is less than k_c. (a) $\omega = 900$ rad/s. (b) $\omega = 800$ rad/s.

forces are eliminated. The ripple of the imparted forces has been substantially suppressed to approximately 10% of the force mean value. Furthermore, it is observed that the greater the actuation speed ω is, the greater the forces applied to the object are.

Hence, designing a manipulator according to the design guidelines presented in Section III results in impulse-free, continuous and controllable forces. A set of further experiments demonstrated that the range of forces the platform exerts on a static object lies within the range [0.01–0.3 N].

V. Conclusion

In this paper, the application of forces by a microrobot employing a novel motion mechanism based on vibration minimotors was studied. Theoretical results and simulations based on a single-dimensional model of the platform–manipulator object system demonstrated the following.

1) The motion mechanism can be used to impart forces on microobjects.
2) The actuator rotational speed can be used as a control variable to regulate the mean value of the force magnitude imparted on an object.
3) The forces exerted on an object can be impulsive or smooth depending on the values of certain structural parameters such as the manipulator stiffness and damping.
4) It was proved mathematically that if certain conditions are met, the manipulator will perform ideal force transmission, i.e., impulse-free, low ripple controllable generation of manipulation forces. These conditions led to corresponding design guidelines.

Force experiments were conducted and the experimental results verified the theoretical results. The experiments demonstrated that the forces, generated by a manipulator designed for ideal force transmission, lie within the range [0.01–0.3 N], and are subject to low ripple, impulse-free and controllable, and thus, applicable to a broad range of micromanipulations.

One may note that there are cases that require forces with an impulsive behavior. Such a case might be the penetration of a cell by a needle-type manipulator. Therefore, as a future work, we intend to design a variable stiffness manipulator, which would lend itself to a broader range of microapplications.

Appendix A

In this Appendix, expressions for variables c_1, c_2, c_3, and c_4, used in Section III are presented

$$\begin{aligned} c_1 =& (kx_0 + g(2m+M)\mu)((b\omega)^2 + (k - M\omega^2)^2) \\ &+ 2kmr\omega^2((k\mu + \omega(b - M\mu\omega))\cos\theta_s'' \\ &+ (-k + \omega(b\mu + M\omega))\sin\theta_s'')) \\ &/(k((b\omega)^2 + (k - M\omega^2)^2)) \end{aligned} \tag{A1}$$

$$\begin{aligned} c_2 =& (b(kx_0 + g(2m+M)\mu)((b\omega)^2 + (k - M\omega^2)^2) \\ &+ 2kmr\omega^2((b^2\omega + 2M\omega(-k + M\omega^2) \\ &+ b\mu(k + M\omega^2))\cos\theta_s'' \\ &+ (b^2\mu\omega + 2M\mu\omega(-k + M\omega^2) - b(k + M\omega^2))\sin\theta_s'')) \\ &/(k\sqrt{-b^2 + 4kM}((b\omega)^2 + (k - M\omega^2)^2)) \end{aligned} \tag{A2}$$

$$\begin{aligned} c_3 =& ((k(x_0 + x_1) - g(2m+M)\mu)((b\omega)^2 + (k - M\omega^2)^2) \\ &+ 2kmr\omega^2((-k\mu + \omega(b + M\mu\omega))\cos(\theta_f'' + \theta_s'') \\ &- (k + \omega(b\mu - M\omega))\sin(\theta_f'' + \theta_s''))) \\ &/(k((b\omega)^2 + (k - M\omega^2)^2)) \end{aligned} \tag{A3}$$

$$\begin{aligned} c_4 =& (b(k(x_0 + x_1) - g(2m+M)\mu)((b\omega)^2 + (k - M\omega^2)^2) \\ &+ 2kmr\omega^2((b^2\omega + 2M\omega(-k + M\omega^2) - b\mu(k \\ &+ M\omega^2))\cos(\theta_f'' + \theta_s'') - (b^2\mu\omega + 2M\mu\omega(-k + M\omega^2) \\ &+ b(k + M\omega^2))\sin(\theta_f'' + \theta_s''))) \\ &/(k\sqrt{-b^2 4kM}((b\omega)^2 + (k - M\omega^2)^2)). \end{aligned} \tag{A4}$$

References

[1] A. Kortschack, A. Shirinov, T. Truper, and S. Fatikow, "Development of mobile versatile nanohandling microrobots: Design, driving principles, haptic control," *Robotica*, vol. 23, no. 4, pp. 419–434, Jul. 2005.
[2] P. Dario, R. Valleggi, M. C. Carrozza, M. C. Montesi, and M. Cocco, "Microactuators for microrobots: A critical survey," *J. Micromech. Microeng.*, vol. 2, pp. 141–157, 1992.
[3] W. Trimmer and R. Jebens, "Actuators for micro robots," in *Proc. IEEE Int. Conf. Robot. Autom. (ICRA 1989)*, Scottsdale, AZ, pp. 1547–1552.
[4] J.-M. Breguet and R. Clavel, "Stick and slip actuators: Design, control, performances and applications," in *Proc. Int. Symp. Micromech. Human Sci. (MHS)*. Nagoya, Japan, 1998, pp. 89–95.
[5] F. Schmoeckel and S. Fatikow, "Smart flexible microrobots for scanning electron microscope (SEM) applications," *J. Intell. Mater. Syst. Struct.*, vol. 11, no. 3, pp. 191–198, 2000.
[6] F. Schmoeckel and H. Worn, "Remotely controllable mobile microrobots acting as nano positioners and intelligent tweezers in scanning electron microscopes (SEMs)," in *Proc. Int. Conf. Robot. Autom. (ICRA 2001)*, Seoul, Korea, pp. 3903–3913.
[7] B. Roland, Z. Wolfgang, and C. Alain, "Inertial drives for micro- and nanorobots: Analytical study," in *Proc. SPIE Photon. East 1995:*

Microrobot. Micromech. Syst. Symp., vol. 2593, Bellingham, L. E. Parker, Eds. Philadelphia, PA: SPIE.

[8] C. Alain, Z. Wolfgang, B. Roland, and S. Roland, "A robot system for automated handling in micro-world," in *Proc. Int. Conf. Intell. Robots Syst. (IROS 1995)*, Pittsburgh, PA, 2008, pp. 3185–3191.

[9] S. Martel, M. Sherwood, C. Helm, W. Garcia de Quevedo, T. Fofonoff, R. Dyer, J. Bevilacqua, J. Kaufman, O. Roushdy, and I. Hunter, "Three-legged wireless miniature robots for mass-scale operations at the sub-atomic scale," in *Proc. ICRA 2001*, Seoul, Korea, pp. 3423–3428.

[10] S. Martel, "Special surface for power delivery to wireless micro-electro-mechanical systems," *J. Micromech. Microeng.*, vol. 15, pp. S251–S258, 2005.

[11] U. Simu, "Piezoactuators for miniature robots," Doctoral dissertation, Dept. Mater. Sci., Uppsala Univ., Uppsala, Sweden, 2002.

[12] U. Simu and S. Johansson, "Fabrication of monolithic piezoelectric drive units for miniature robot," *J. Micromech. Microeng.*, vol. 12, pp. 582–589, 2002.

[13] J. Brufau, M. Puig-Vidal, J. Lopez-Sanchez, J. Samitier, W. Driesen, J. Brequet, N. Snis, S. Urban, S. Johansson, T. Velten, J. Seyfried, R. Estana, and H. Woern, "MICRON: Small autonomous robot for cell manipulation applications," in *Proc. IEEE ICRA 2004*, Barcelona, Spain, pp. 844–849.

[14] P. Vartholomeos, S. Loizou, M. Thiel, K. Kyriakopoulos, and E. Papadopoulos, "Control of the multi agent micro-robotic platform MuiCRoN," in *Proc. 2006 IEEE Int. Conf. Control Appl.*, TUM, Munich, pp. 1414–1419.

[15] P. Vartholomeos and E. Papadopoulos, "Analysis, design and control of a planar micro-robot driven by two centripetal-force actuators," in *Proc. IEEE ICRA 2006*, Orlando, FL, pp. 649–654.

[16] P. Vartholomeos and E. Papadopoulos, "Dynamics, design and simulation of a novel micro-robotic platform employing vibration micro-actuators," *ASME J. Dyn. Syst., Meas. Control*, vol. 128, no. 1, pp. 122–133.

[17] Z. Lu, P. C. Chen, and W. Lin, "Force sensing and control in micromanipulation," *IEEE Trans. Syst., Man, Cybern. C, Appl. Rev.*, vol. 36, no. 6, pp. 713–724, Nov. 2006.

[18] J. J. Gorman and N. G. Dagalakis, "Probe-based micro-scale manipulation and assembly using force feedback," in *Proc. 1st Joint Emerg. Preparedness Response/Robot. Remote Syst. Top. Meeting*. Salt Lake City, UT, Feb. 11–16, 2006, pp. 621–628.

[19] H. Zhang, Y. Bellouard, E. Burdet, R. Clavel, A. Poo, and W. Hutmacher, "Shape memory alloy microgripper for robotic microassembly of tissue engineering scaffolds," in *Proc. IEEE ICRA 2004*, Barcelona, Spain, pp. 4918–4923.

[20] L. Sciavicco and B. Siciliano, *Modelling and Control of Robot Manipulators*. New York: Springer-Verlag, 2001.

Panagiotis Vartholomeos (S'04–M'08) received the M.Eng. degree in electrical and electronic engineering from Imperial College London, London, U.K., in 2001, and the Ph.D. degree in mechanical engineering from the National Technical University of Athens (NTUA), Athens, Greece, in 2007.

He is currently with the Department of Mechanical Engineering, NTUA. His current research interests include microrobotics, robotics, control and modeling of dynamic systems.

Dr. Vartholomeos is a member of the Technical Chamber of Greece (TEE).

Evangelos Papadopoulos (S'83–M'91–SM'97) received the Diploma in mechanical engineering from the National Technical University of Athens (NTUA), Athens, Greece, in 1981, and the M.S. and Ph.D. degrees from Massachusetts Institute of Technology (MIT), Cambridge, in 1983 and 1991, respectively, all in mechanical engineering.

From 1985 to 1987, he was an Analyst at the Hellenic Navy, Athens. In 1991, he joined McGill University and the Centre for Intelligent Machines (CIM) as an Assistant Professor and was tenured in 1997. He is currently a Professor in the Department of Mechanical Engineering, NTUA. He is engaged in the areas of systems, controls, mechatronics, and robotics. He is the author or coauthor more than 150 published technical articles in journals and refereed conference proceedings. He is as an Associate Editor of the *Machine and Mechanism Theory*. His current research interests include the area of robotics, modeling and control of dynamic systems, and mechatronics and design.

Dr. Papadopoulos is a Senior Member of the American Institute of Aeronautics and Astronautics (AIAA) and a member of the American Society of Mechanical Engineers (ASME), the Technical Chamber of Greece, and the Sigma Xi. He is as an Associate Editor of the IEEE TRANSACTIONS ON ROBOTICS. He was a Guest Editor of the IEEE/ASME TRANSACTIONS ON MECHATRONICS.